APPLIED PHYSICS

Gradual labeling with fluorogenic probes: A general method for MINFLUX imaging and tracking

Longfang Yao[1,2]†, Dongjuan Si[3]†, Liwen Chen[4], Shu Li[1,2], Jiaxin Guan[1,2], Qiming Zhang[1,2], Jing Wang[1,2], Jiong Ma[4]*, Lu Wang[3]*, Min Gu[1,2]*

Minimal photon fluxes (MINFLUX) nanoscopy excels in nanoscale protein studies but lacks a universal method for simultaneous imaging and live-cell tracking in dense cellular environments. Here, we developed a general strategy, gradual labeling with fluorogenic probes for MINFLUX (GLF-MINFLUX) imaging and tracking. In GLF-MINFLUX, membrane-permeable small-molecule fluorogenic dye with protein-induced "off/on" switching is gradually labeled, located, and bleached, enabling sequential positioning and tracking of individual proteins. GLF-MINFLUX reveals continuous microtubules with 2.6-nanometer localization precision, offering substantially improved precision (1.7-fold), acquisition (2.2-fold), and target density (3-fold) compared to conventional MINFLUX with Alexa Fluor 647. GLF-MINFLUX also enabled the three-dimensional localization of translocase of the outer mitochondrial membrane 20 proteins within mitochondrial clusters and dual-channel nanoscale imaging of endogenous neuronal microtubules and microfilaments. GLF-MINFLUX allowed live-cell single-protein tracking with 7.8-nanometer precision at ~200-microsecond temporal resolution, revealing distinct diffusion behaviors and rates between the basal membrane and filopodia. GLF-MINFLUX, requiring only tuning of probe concentration, offers molecular-level insights into protein functions.

INTRODUCTION

Fluorescence nanoscopy has revolutionized the study of protein functions in cellular activities by providing nanoscale spatial details of individual proteins. Minimal photon fluxes (MINFLUX) nanoscopy, in particular, has set a standard for localization precision, achieving a localization precision of ~2 nm and a submillisecond temporal resolution (*1*–*7*). This technique localizes emitters using a doughnut-shaped excitation beam that moves around a probing area, recording photon fluxes at each position (*3*). In each iteration, the scanning area is progressively narrowed, and the beam's center aligns more precisely with the emitter's location. By superimposing the precise positions of targets, MINFLUX generates high-resolution images with both exceptional spatial and temporal precisions.

However, as MINFLUX pushes the resolution of imaging and tracking to molecular level, the labeling method and the fluorophores used to tag target proteins have become the key bottlenecks in determining the quality and effectiveness. According to the principles of MINFLUX, MINFLUX localization requires only one labeled emitter within the doughnut-shaped excitation beam; two or more emitters cause invalid localization (Fig. 1A). During localization, the system evaluates the ratio of photon counts at the center (n_0) versus the edges (n_1 to n_6) of the beam, termed the center frequency ratio (CFR), to determine the number of emitters. If the CFR falls below a predefined threshold, then it indicates the presence of a single emitter, leading to valid localization; otherwise, it is marked as invalid (Fig. 1A and Tables 1 to 3). However, there is a risk that an ensemble of multiple emitters simulating the luminescent behavior characteristic of a single molecule could lead to decreased localization precision. Invalid localizations compromise the positional integrity of target structures and considerably prolong the total image acquisition time or stopped the single-molecule tracking.

The challenge of fluorescent labeling for the MINFLUX imaging and tracking becomes even more pronounced in densely packed cellular structures, such as cytoskeletons and membrane proteins, which are essential for regulating vital cellular activities but remain difficult to study at the molecular level. Conventional MINFLUX nanoscopy relies on organic fluorophores such as Alexa Fluor 647, which exhibit stochastic blinking ("on/off" switching behavior) in the presence of reductive and oxidative buffer solutions and activation lasers (*8*). Although widely used, these fluorophores typically have an on/off duty cycle exceeding 0.0005, meaning that one fluorescence event occurs per 2000 molecules (*8*). Therefore, the labeling density in MINFLUX must not exceed the inverse of the duty cycle to ensure proper localization during the imaging process (Fig. 1B). In densely packed structures such as axonal microtubules, where up to 8000 targets may be present (text S1 and fig. S1), this high density leads to multiple active emitters and frequent invalid localizations and single-molecule tracking. The hydrophilic sulfonate moiety of Alexa Fluor 647 restricts its membrane permeability, hindering its ability to effectively track intracellular proteins in living cells. Moreover, several targets fall within the localization precision limit, resulting in extensive overlap of localization clouds from distinct entities (Fig. 1C). These so-called localization clouds are generated as a single emitter undergoes multiple localizations from the start of the localization process until quenching, with the localization centers arranged similarly to an electron cloud (*9*). Furthermore, the repeated on/off cycling of blinking dyes creates redundant and confluent localization clouds, impeding accurate localization in MINFLUX. These

[1]School of Artificial Intelligence Science and Technology, University of Shanghai for Science and Technology, 516 Jungong Road, Shanghai 200093, China. [2]Institute of Photonic Chips, University of Shanghai for Science and Technology, 516 Jungong Road, Shanghai 200093, China. [3]MOE Key Laboratory of Smart Drug Delivery, MOE Innovative Center for New Drug Development of Immune Inflammatory Diseases, School of Pharmacy, Fudan University, Shanghai 200433, China. [4]Department of Optical Science and Engineering, Shanghai Engineering Research Center of Ultra-precision Optical Manufacturing, Fudan University, 220 Handan Road, Shanghai 200433, China.
*Corresponding author. Email: jiongma@fudan.edu.cn (J.M.); lwangfd@fudan.edu.cn (L.W.); gumin@usst.edu.cn (M.G.)
†These authors contributed equally to this work.

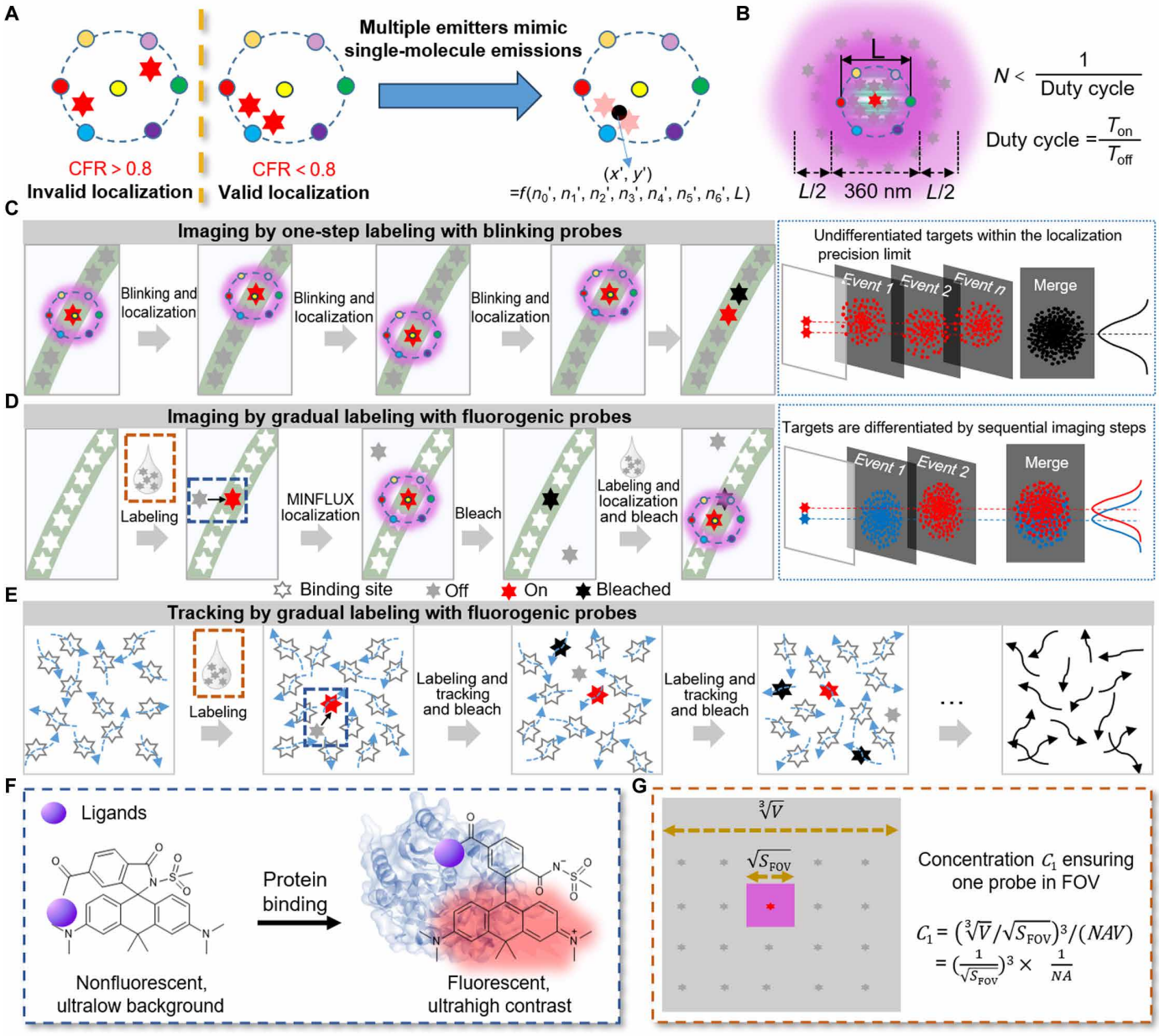

Fig. 1. Schematic diagram illustrating the working principles of conventional MINFLUX and GLF-MINFLUX nanoscopy. (**A**) Scenario within the doughnut-shaped detection area where multiple fluorophores cause invalid localization or mimic the behavior of a single fluorophore. (**B**) The outline of the extent of the doughnut's movement in the localization procedure. *N* signifies the count of active dye molecules contributing effectively within this movement range. T_{on} and T_{off} refer to the durations during which individual dye molecules are in their fluorescent on and off states, respectively. (**C**) Working principle of MINFLUX nanoscopy relying on one-step labeling with blinking probes such as Alexa Fluor 647, demonstrating its challenges, namely, with regard to the undistinguishedness of targets within the localization precision limit. (**D**) Working mechanism of GLF-MINFLUX imaging. Each target protein undergoes labeling-locating-bleaching events, thus allowing for the chronological segregation and precise positioning of targets within the localization precision limit. (**E**) Working principle of MINFLUX tracking. (**F**) "Off/on" switching process of fluorogenic probe MaP618m before and after binding to the target protein. (**G**) Schematic representation detailing the computational methodology for determining probe concentration C_1. Diameter of the beam displacement (*L*), area of the imaging field of view (S_{FOV}), Avogadro's constant (*NA*), and volume (*V*).

overlapping clouds remain difficult to resolve by MINFLUX's unregulated on/off switching, even with complex clustering algorithms that assigns localization clouds to individual molecules (*9*).

To overcome these challenges in MINFLUX imaging and tracking, a straightforward method is needed to control the on/off switching behavior, particularly the number of "swi fluorescent targets. While the development of organic dyes with smaller on/off duty cycles or photoactivatable probes has the potential to mitigate some of these issues, it requires intricate synthesis and optimization processes (*10*–*14*). In addition, DNA-based point accumulation for imaging in nanoscale topography (DNA-PAINT) has been smartly used to avoid the regulation of the on/off switching process and

Table 1. The critical parameters for the 2D imaging iteration sequence of MINFLUX. The minimal photon count is the number of photons required to be accumulated during iteration to ensure sufficiently high positioning accuracy of the system in theory. When CFR is displayed as "off," it means that there is no constraint on CFR for that iteration. The laser power factor is the ratio of the laser power during iteration to the set power.

Iteration	*L* (nm)	Minimal photon count	CFR limit	Laser power factor
Prelocalization		160	Off	1
1	288	150	Off	1
2	151	100	0.8	2
3	76	100	0.8	4
4	40	150	Off	6

Table 2. The critical parameters for the 3D imaging iteration sequence of MINFLUX.

Iteration	*L* (nm)	Minimal photon count	CFR limit	Laser power factor
Prelocalization		160	Off	1
1	288	400	Off	1
2	288	100	Off	1
3	288	50	Off	1
4	151	67	0.9	2
5	151	33	Off	2
6	76	67	0.8	4
7	76	33	Off	4
8	40	100	Off	6
9	40	50	Off	6

Table 3. The critical parameters for the tracking iteration sequence of MINFLUX.

Iteration	*L* (nm)	Minimal photon count	CFR limit	Laser power factor
Prelocalization		40	Off	1
1	302	20	Off	1
2	151	20	0.8	2
3	100	20	Off	3

enable three-color MINFLUX nanoscopy of mitochondria (*5*). MINFLUX technology requires only a small number of photons (only 20) for precise localization (*15*), making it highly susceptible to interference from weak background noise. In DNA-PAINT MINFLUX, background noise from diffusing imager strands is mitigated by reducing the pinhole diameter, which, however, extends the imaging duration (*5*). The advancement of fluorogenic DNA probes (*16*), orthogonal DNA sequences, reduction in label sizes, and refinement of wash-label procedures have continuously pushed the capabilities of DNA-PAINT MINFLUX nanoscopy, making it feasible to image densely packed structures (text S2 and table S1) (*5*, *17*). However, single-protein tracking using DNA-PAINT in live-cell MINFLUX nanoscopy is currently impossible because of the difficulty of introducing impermeable exogenous DNA probes into living cells.

To overcome this challenge, we have devised a versatile strategy known as gradual labeling with fluorogenic probes for MINFLUX (GLF-MINFLUX) imaging and tracking. We applied the membrane-permeable MaP dye that undergoes protein-induced "off/on" switching (*18*), allowing for stepwise labeling, localization, and bleaching of individual proteins in densely packed structures. Compared to conventional MINFLUX using Alexa Fluor 647, GLF-MINFLUX reveals continuous microtubules with an impressive localization precision of 2.6 nm and a notable improvement in precision, acquisition speed, and target density. Moreover, GLF-MINFLUX enabled the three-dimensional (3D) localization of translocase of the outer mitochondrial membrane 20 (TOM20) proteins within mitochondrial clusters, as well as dual-channel nanoscale imaging of endogenous neuronal microtubules and microfilaments. Notably, GLF-MINFLUX tracking of single protein at the membrane provides

a remarkable 7.8-nm precision at a temporal resolution of 200 μs, uncovering distinct diffusion behaviors and rates between the basal membrane and filopodia.

RESULTS

Design and working principles of GLF-MINFLUX

To effectively control the on/off switching process for MINFLUX nanoscopy, we propose adopting a gradual labeling method with fluorogenic probes (GLF-MINFLUX) and only varying the probe concentration to regulate the number of on fluorescent targets (Fig. 1, D and E). In GLF-MINFLUX, low-concentration (approximately picomolars) probes were applied to sparsely illuminate target proteins, with each undergoing labeling-locating-bleaching events using MINFLUX, forming a cycle. This cycle repeats with additional probes until all targets are precisely localized and tracked. Densely packed structures are segmented into sparsely labeled subgroups, allowing sequential nanoscale imaging and tracking via MINFLUX with substantially reduced invalid localizations.

This gradual labeling process needs to be performed under wash-free conditions and thus requires probes with ultralow background fluorescence, even after multiple labeling cycles, while displaying bright fluorescence upon binding to target proteins. Meanwhile, the labeled probe should be cell permeable, allowing intracellular protein imaging and tracking. We, thus, used highly fluorogenic, cell-permeable MaP probes (*18*), which are nonfluorescent spirocyclic compounds in their unbound state and transition into fluorescent zwitterions upon binding to target proteins (Fig. 1F). The protein-induced off/on switching process and exceptional fluorogenicity yield high-contrast imaging for single-molecule localization without necessitating the washing out of excess probes, specific buffer systems, or dedicated activation lasers. We conjugated highly fluorogenic MaP618m with chloroalkane, cabazitaxel, and jasplakinolide for labeling HaloTag, microtubules, and microfilaments, res pectively, for GLF-MINFLUX nanoscopy (text S3, table S2, and figs. S3 to S6).

To ensure single-molecule localization, we calculated the theoretical probe concentration (C_1) required for a single emitter within the field of view as $C_1 = \left(\frac{1}{\sqrt{S_{FOV}}}\right)^3 \times \frac{1}{NA}$ (Fig. 1G and texts S4 and S5). This formula does not account for probe diffusion. Considering that the free probes in the solution decrease over the course of imaging, the actual used concentration is slightly elevated above C_1. Furthermore, the probe solution is refreshed at regular intervals during the imaging process to enhance the imaging efficiency and reduce the overall imaging duration. For tracking applications, considering the lower photon requirement compared to imaging, low-power laser illumination is used to extend tracking time, thereby increasing the exposure time per emitter relative to imaging conditions.

Comparison of MINFLUX with GLF-MaP dyes and Alexa Fluor 647

To demonstrate the applicability of GLF-MINFLUX for nanoscale imaging of densely packed microtubules, we stained tubulin-HaloTag–expressing BS-C-1 cells with the reported MaP618m-Halo with high fluorogenicity (*18*). In GLF-MINFLUX, 100 pM MaP618m-Halo was incubated until the localization count saturated in each cycle, with cycles repeated until all targets were labeled. GLF-MINFLUX enabled nanoscale imaging of intact microtubules (Fig. 2A and fig. S7), whereas one-step labeling with Alexa Fluor 647, used as a control, only produced discontinuous lines of microtubules (Fig. 2B and fig. S7).

Consistent with prior studies (*4*), MINFLUX imaging with Alexa Fluor 647 used a laser power of 49 μW, resulting in a photon count of 5084 and 9.1 localizations within a localization cloud, exceeding the minimum of five localizations required to ensure the accuracy of the localization precision (text S6 and figs. S8 and S9) (*5*). Notably, GLF-MINFLUX with MaP618m-Halo allowed for the approximately sixfold stronger laser power of 293 μW, resulting in a photon count of 14,103 while maintaining 11.9 localizations per localization cloud and a 2.7-fold increase in photon count (figs. S8 and S9). According to the formula for MINFLUX localization precision, the increased photon counts contributed positively to improved localization precision. Upon detecting individual fluorescent molecules, MaP618 exhibited stable emission, approximately 1.5 times higher than Alexa Fluor 647 (fig. S10), aiding in improved localization precision. Consistent with single-molecule behavior, the photon emission from MaP618m remained relatively stable throughout the imaging process, with minimal variations between localization points (Fig. 2C). In contrast, Alexa Fluor 647 exhibited even greater variability than that from the optical fluctuation of single molecule (Fig. 2D), which may be due to high labeling density causing multiple emitters to be defined as single-molecule emissions (Fig. 1A). Overall, these factors enabled GLF-MINFLUX to achieve an impressive localization precision of 2.6 nm, which is 1.7 times higher than that obtained with Alexa Fluor 647 in MINFLUX (Fig. 2E).

Meanwhile, GLF-MINFLUX shows a threefold higher target density than MINFLUX with Alexa Fluor 647 (Fig. 2F), showing greater efficiency in revealing the integrity of linear microtubule structures. MINFLUX imaging of microtubules can be finished within 1.5 hours using gradual labeling of MaP618m-Halo, demonstrating a 2.2-fold increase in the acquisition rate (Fig. 2G, fig. S11, and movies S1and S2). In addition, GLF-MINFLUX with MaP618m-Halo displays a 1.2-fold increase in the CFR (Fig. 2H), a 1.8-fold decrease in the time between valid events (t_{btw}) (Fig. 2I), and a 1.5-fold decrease in the background emission frequency (f_{bg}) (Fig. 2J) (*5*). These results underscore the feasibility of GLF-MINFLUX and its superior performance in nanoscale imaging of microtubules compared to conventional MINFLUX with Alexa Fluor 647.

Mapping of TOM20 within clusters via 3D GLF-MINFLUX

Inspired by the exceptional performance of GLF-MINFLUX, we next explored its feasibility in mapping targets within densely packed structures in three dimensions. The TOM complex serves as the primary import channel for nuclear-encoded proteins into the mitochondria. Multiple TOM20 proteins aggregate to form clusters, yet the spatial distribution within a single cluster remains poorly understood (*19*). Here, we used GLF-MINFLUX to image TOM20 within 3D clusters at the nanoscale. Initial experiments assessed the influence of probe concentration on image quality and labeling rate by staining fixed TOM20-Halo–expressing BS-C-1 cells with varying concentrations of fluorogenic MaP618m-Halo, ranging from 50 pM to 1 nM (fig. S12). Minimal background signal was observed with wash-free imaging, yielding signal-to-noise ratios of up to 24.7, even at a minimal probe concentration of 50 pM (fig. S12). Mitochondrial TOM20 staining persisted for 13 to 20 min (fig. S12), ensuring effective separation and localization of single molecules in each cycle during GLF-MINFLUX.

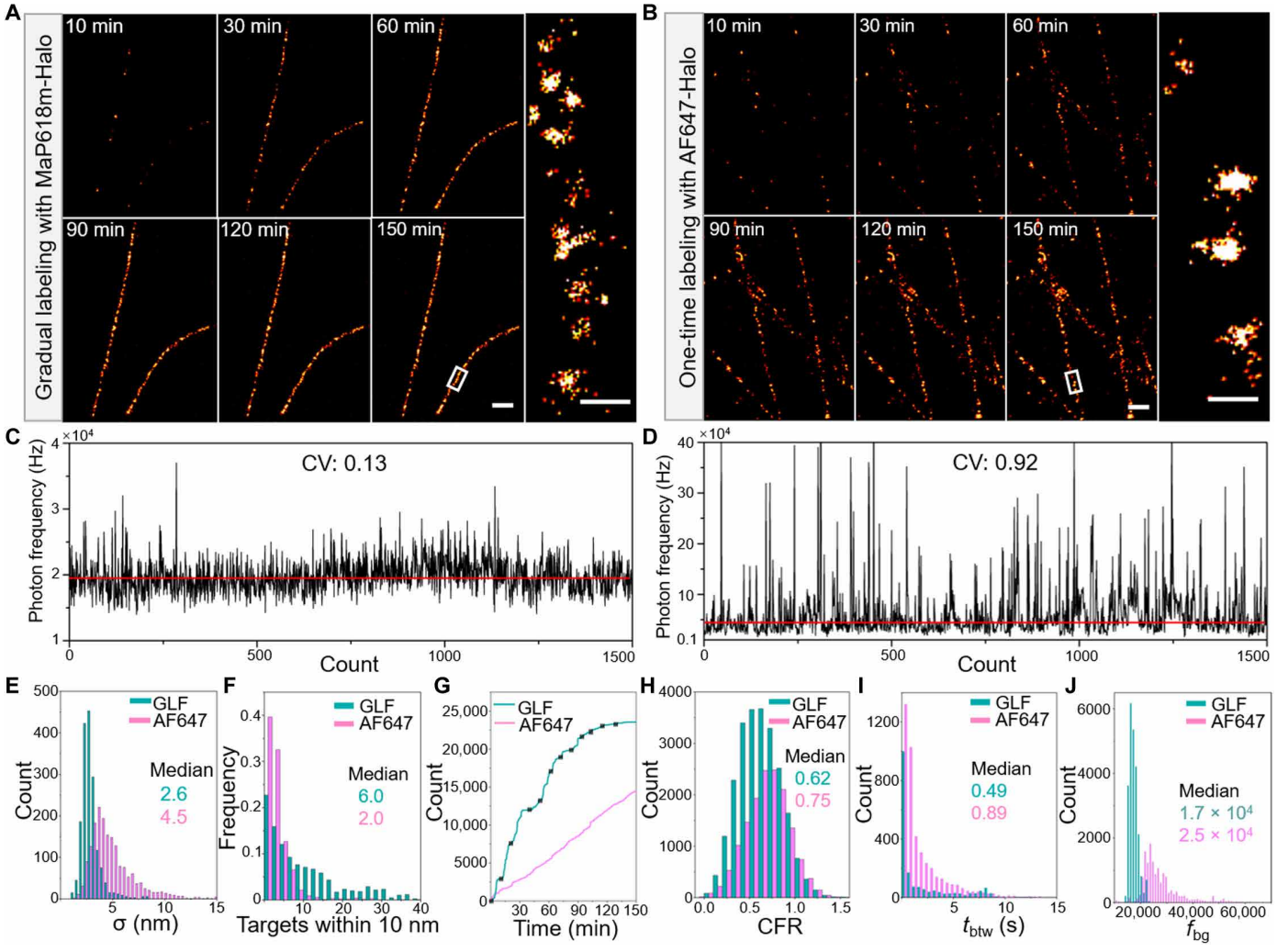

Fig. 2. 2D GLF-MINFLUX nanoscopy of microtubules. (**A**) GLF-MINFLUX images of microtubules in Halo–enhanced green fluorescent protein (EGFP)–tubulin–expressing BS-C-1 cells after gradual labeling with MaP618m-Halo at various time points. The inset on the right shows a magnified version of the region marked by the white box in the 150-min image. (**B**) MINFLUX images of microtubules in Halo-EGFP-tubulin–expressing BS-C-1 cells at various time points after one-step labeling with Alexa Fluor 647 (AF647). The inset on the right shows a magnified version of the region marked by the white box in the 150-min image. (**C** and **D**) Photon emission frequency over time for 1500 localizations using GLF-MINFLUX and Alexa Fluor 647. Coefficient of variation (CV), the ratio of standard deviation to the mean of the original data. (**E**) Histogram of the localization precision of labeled tubulins in each image obtained using GLF-MINFLUX with MaP618m-Halo or MINFLUX with Alexa Fluor 647–Halo ($n = 5$ images of each type). (**F**) The number of targets within a 10-nm radius around each target. (**G** to **J**) Comparative analysis of GLF-MINFLUX with MaP618m-Halo and MINFLUX nanoscopy with Alexa Fluor 647 in terms of imaging speed (G), CFR (H), t_{btw} (I), and f_{bg} (J). CFR reflects the indicator of the likelihood of multiple emitters occurring during localization, t_{btw} reflects reflecting the time for recording images, and f_{bg} reflects the frequency of invalid localization between valid. The black dots in (G) indicate additions of new probes. Scale bars, 500 nm [(A) and (B)] and 50 nm [(A) and (B), inset].

We then performed GLF-MINFLUX nanoscopy on TOM20 stained with MaP618m-Halo (text S8) and successfully obtained nanoscale images of TOM20 proteins with axial and lateral localization precisions of 2.3 and 3.5 nm, respectively (Fig. 3, A and B, fig. S13, and movie S3). 3D-GLF-MINFLUX revealed a dense distribution of TOM20 in mitochondria, which reveals homogeneous and heterogeneous spread across the mitochondrial outer membrane (Fig. 3C and fig. S14). This could arise from differences in protein expression or cellular stress responses (*20*, *21*). Moreover, more than 7.9 ± 6 HaloTag-fused TOM20 proteins were detected within each cluster, with spatial separations ranging from 2.7 to 18.5 nm according to the 3D distribution (Fig. 3, D and E). Notably, the measured separation distance of 2.7 nm, which surpasses the localization precision of 3.7 nm (table S3), underscores its resolving capability to distinguish proximal targets below the precision limit (*1*, *22*). This is challenging to achieve in conventional MINFLUX with Alexa Fluor 647 due to the frequent multicycle on-off switching of individual fluorophores, even when clustering algorithms analysis is performed (*9*).

GLF-MINFLUX nanoscopy of the endogenous cytoskeleton

To ensure an accurate representation of real samples in imaging data, we prefer endogenous cellular proteins with small-size labels in MINFLUX nanoscopy. Consequently, commonly used antibodies and nanobodies ranging from 5 to 10 nm in size are too large for MINFLUX imaging with ~2-nm localization precision (Fig. 4A). To address the problem in label size, we conjugated fluorogenic

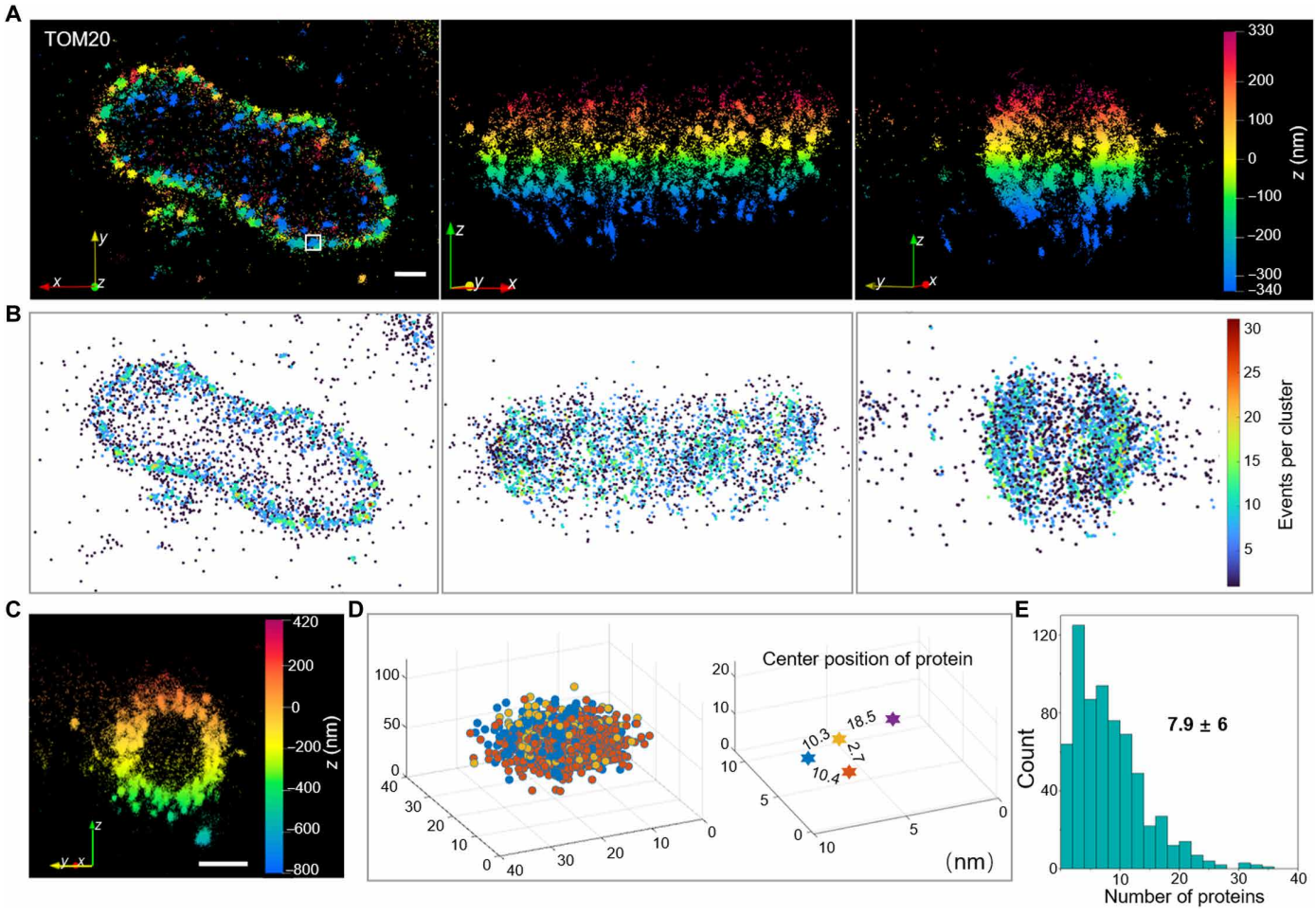

Fig. 3. 3D GLF-MINFLUX nanoscopy of mitochondrial TOM20 clusters. (**A**) 3D GLF-MINFLUX imaging of TOM20 fused with HaloTag labeled with MaP618m-Halo in the mitochondria of HeLa cells. The *z*-dimension information is color coded according to the color scale bar. (**B**) Scatter plot illustrating the central positions of each emitter corresponding to the respective fields of view in (A). The color bar variations denote the number of targets within each cluster. (**C**) Axial projection view of TOM20 clusters with homogeneous spread across the mitochondrial outer membrane. (**D**) 3D distribution of the clusters of TOM20 within the white box in (A). Each dot represents a location, with colors indicating different localization clouds. The stars on the right represent the central points of the corresponding localization cluster on the left. (**E**) Protein count of TOM20-HaloTag within each TOM cluster ($N = 8$ images). Scale bars, 200 nm.

MaP618m with cabazitaxel and jasplakinolide to create MaP618m-tubulin and MaP618m-actin, enabling direct and robust binding to endogenous microtubules and microfilaments without the need for protein tags, antibodies, or nanobodies (Fig. 4A). Upon MaP618m-tubulin binding to microtubules, a remarkable 46-fold increase in absorbance at 618 nm and an unprecedented 217-fold increase in fluorescence at 634 nm were observed (Fig. 4B). Meanwhile, wash-free imaging of BS-C-1 cells with MaP618m-tubulin, even at concentrations as high as 500 nM, had negligible background noise and an outstanding signal-to-noise ratio of 312 (fig. S15). Similarly, wash-free imaging of BS-C-1 cells with MaP618m-actin enabled gradual labeling within 20 min and demonstrated an impressive signal-to-noise ratio of 221 (fig. S16).

We next evaluated the feasibility of MaP618m-tubulin and MaP618m-actin in GLF-MINFLUX nanoscopy of the endogenous microtubules and microfilaments. GLF-MINFLUX nanoscopy with the highly fluorogenic MaP618m-tubulin showed intact structures of microtubules (Fig. 4, C and D). The high density of labeled fluorophores enables imaging an average peak-to-peak distance between microtubule sidewalls of 22.4 ± 7 nm (Fig. 4, D and E), consistent with reported diameters in the literature (*23*). In addition, the average photon counts per MaP618m-tubulin molecule reached 17,798 (Fig. 4F), comparable to that from MaP618m-Halo (fig. S9). Furthermore, GLF-MINFLUX imaging with the fluorogenic MaP618m-actin successfully revealed endogenous, densely packed microfilaments in HeLa cells. It yielded 2.1 localization events within a 10-nm radius around each target and 4.2 localization precision in the microfilaments of pseudopodia, producing 1.6- and 1.2-fold improvements compared to conventional MINFLUX imaging with Alexa Fluor 647 (Fig. 4, G to J, and table S3). These results demonstrate the feasibility of nanoscale imaging of endogenous cytoskeleton via GLF-MINFLUX with MaP618m-tubulin and MaP618m-actin.

Dual-channel GLF-MINFLUX of the endogenous neuronal axonal cytoskeleton

The neuronal axonal cytoskeleton is vital for controlling cellular functions such as cell division, migration, intracellular trafficking, and signal transduction. However, the dense and intricately bundled

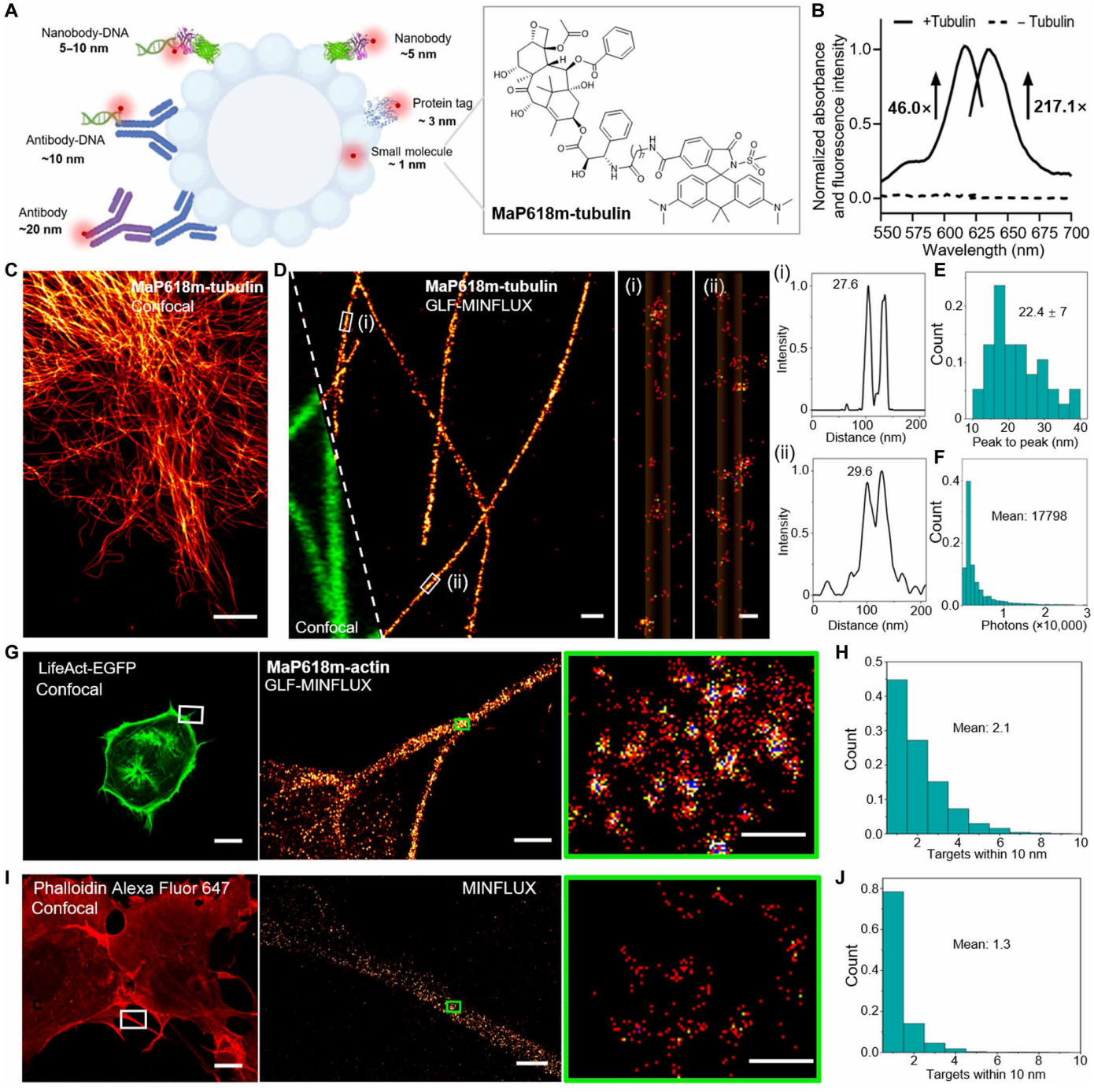

Fig. 4. 2D GLF-MINFLUX nanoscopy of the endogenous microtubules and microfilaments. (**A**) Structure of fluorogenic MaP618m coupled with cabazitaxel for binding to microtubules. (**B**) Absorption and emission spectra of MaP618m-tubulin (1 μM) measured in the presence and absence of tubulin (2 mg/ml) after a 2-hour incubation at 37°C. The annotations in (B) indicate the increased ratios of the absorbance at 616 nm and the fluorescence intensity at 634 nm (λ_{ex} = 590 nm) in the presence and absence of microtubules. (**C**) Confocal image of BS-C-1 cells labeled with 500 nM MaP618m-tubulin under wash-free conditions. (**D**) GLF-MINFLUX imaging of microtubules in fixed BS-C-1 cells labeled with MaP618m-tubulin. The right panels are magnified images corresponding to the white boxes on the left. Gaussian fitting curves of microtubules in (i) and (ii) are also presented on the right. (**E** and **F**) Histogram of peak-to-peak distances and photon count histogram of microtubules in (D). (**G** and **I**) Confocal and MINFLUX imaging of pseudopodia in fixed HeLa cells labeled with MaP618m-actin (G) and Alexa Fluor 647 (I). The right panels are magnified images corresponding to the green boxes on the left. (**H** and **J**) The number of targets within a 10-nm radius around each target in [(H) and (J)]. Scale bars, 10 μm [(C), (G), and (I), confocal], 500 nm [(D), (G), and (I), MINFLUX], 20 nm [(D), MINFLUX close-up], and 50 nm [(G) and (I), MINFLUX close-up].

arrangement of microtubules and microfilaments remains difficult to image with MINFLUX nanoscopy (*17*, *24*). Moreover, conventional large-size antibody-conjugated probes are often limited by constrained imaging resolution and minimal penetration into the confined interstitial spaces around bundled microtubules (*25*). We, thus, used MaP618m-tubulin for GLF-MINFLUX nanoscopy of rat hippocampal neurons, which enabled the observation of more than nine individual microtubules within a single neuron (Fig. 5, A to C). GLF-MINFLUX nanoscopy also reveals microtubules with a diameter of 24 ± 5 nm and the interline spacing of 63 ± 17 nm, consistent with the reported work by electron microscopy (*26*). In addition, the density heatmap centered on each probe indicated that the tubulin density reached 6000 to 14,000/μm^2 (Fig. 5D), higher than the density of around 2000/μm^2 observed for neuronal microtubules labeled with an antibody conjugated to Alexa Fluor 647 (fig. S1 and text S1).

The labeling-locating-bleaching steps of each target in GLF-MINFLUX also facilitated multichannel imaging using only a single excitation laser. Through sequential gradual labeling with the fluorogenic probes MaP618m-tubulin and MaP618m-actin, dual-channel MINFLUX nanoscopic imaging of endogenous microtubules and microfilaments in the axons of rat hippocampal neurons was achieved using only a single 642-nm excitation laser (Fig. 5, E and F). Notably, these dual-channel GLF-MINFLUX images maintained localization precisions of 4.5 and 4.3 nm in each channel after 2 to 3 hours of acquisition, a level of precision in endogenously densely packed structures not reported in previous work to our knowledge.

Single-molecule tracking of membrane dynamics with GLF-MINFLUX in live cells

The diffusion of proteins on cell membranes, including their diffusion rates and underlying models, is critical for cellular functions such as signaling, transport, and communication (*27*). Studies have indicated that diffusion rate and pattern vary depending on membrane regions due to different environment and structure on the membrane. Despite these insights, current methods for tracking

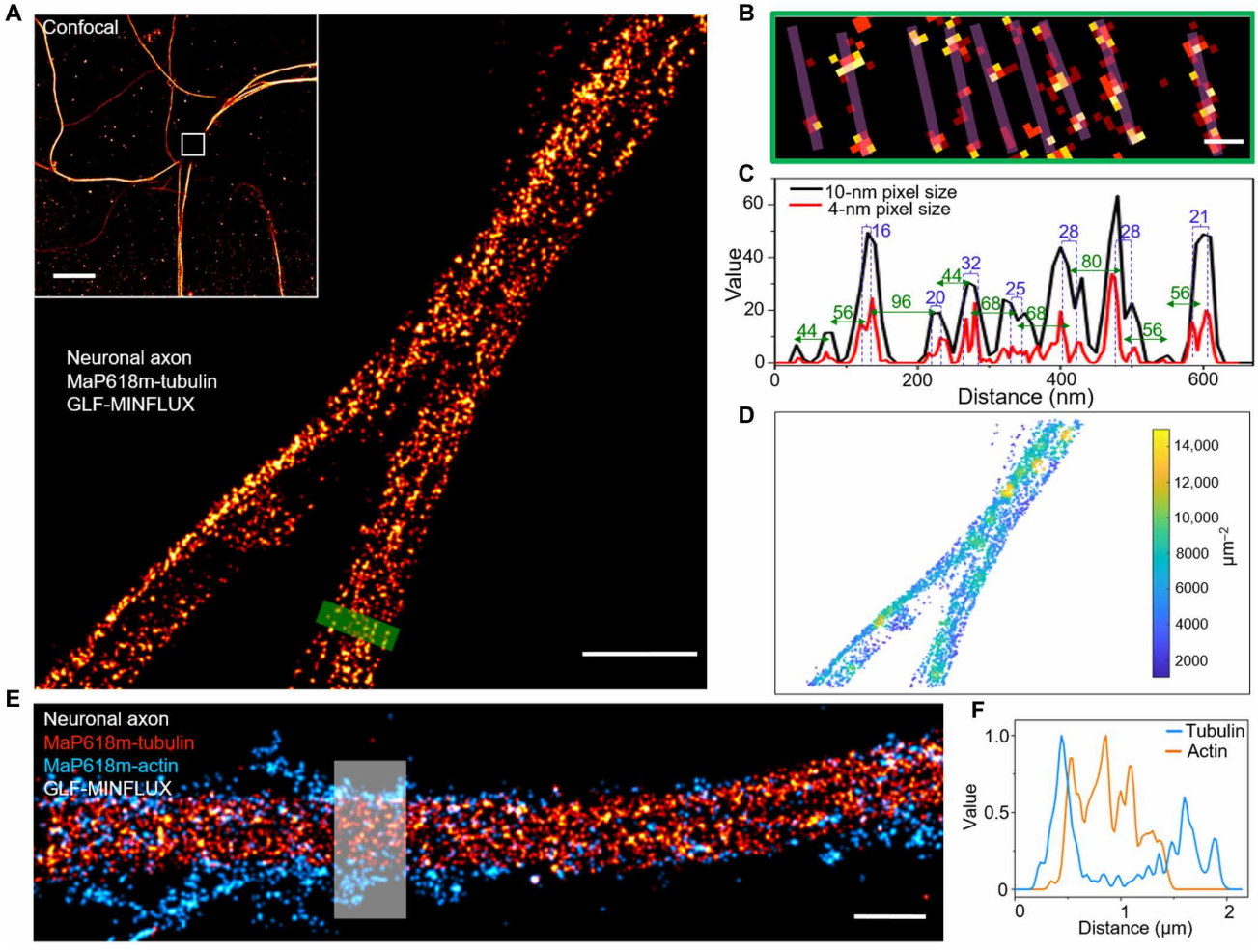

Fig. 5. GLF-MINFLUX nanoscopy of the endogenous neuronal axonal cytoskeleton. (**A**) GLF-MINFLUX image of microtubules in the axons of rat hippocampal neurons labeled with MaP618m-tubulin. The white outlined region in the top-left confocal image denotes the MINFLUX imaging field shown in the larger image. (**B**) An enlargement of the green-striped region in (A) with 10-nm pixel size, showing purple lines indicating the probable trajectories of the microtubules. (**C**) Intensity profiles along the length in (B). (**D**) Density heatmap of microtubules imaged by GLF-MINFLUX in (A). (**E**) Dual-channel MINFLUX images of microtubules and microfilaments in the axons of rat hippocampal neurons labeled with MaP618m-tubulin and MaP618m-actin. The excitation laser wavelength was 642 nm. (**F**) Intensity profiles of microtubules and microfilaments within the white boxed regions of (E). Scale bars, 10 μm [(A), confocal], 1 μm [(A) and (E), MINFLUX], and 50 nm (B).

single-molecule protein movement on membranes face notable limitations, including poor spatiotemporal resolution and challenges in controlling protein expression and labeling in live cells.

To overcome these limitations, we applied GLF-MINFLUX to investigate single-molecule behaviors on living cell membranes. The MaP618m dye, known for its excellent permeability across cell membranes, enabled efficient live-cell labeling at an ultralow concentration of 10 pM with minimal time-varying label density. In our study, we used Halo–enhanced green fluorescent protein (EGFP)–CAAX to label the plasma membrane, where the CAAX sequence—a 19–amino acid peptide from the C terminus of the H-Ras protein—specifically targets and integrates into the plasma membrane, moving with its fluidity (*28*). To assess protein mobility across different membrane regions, we performed single-molecule tracking at the stable basal surface of the cell and at the more dynamic filopodia regions (Fig. 6, A to F).

Using the GLF-MINFLUX approach, we successfully tracked single-molecule trajectories on the membrane (Fig. 6, B and E). GLF-MINFLUX demonstrated exceptional precision in single-molecule tracking, achieving $\sigma_x = 7.9$ nm and $\sigma_y = 7.8$ nm at a temporal resolution of ~200 μs (Fig. 6G). The velocity heatmaps of single-molecule behaviors revealed notable variations in molecular across different areas of the cell base, while movement on filopodia was more uniform (Fig. 6, C and F). Notably, the average diffusion rate (mean squared displacement divided by the time interval) on filopodia was twice as fast as on the basal region (Fig. 6H). In certain trajectories at the cell base, we observed confined and hopping diffusion behaviors: Molecules exhibited slower movement within a specific region before rapidly accelerating and jumping to another area (Fig. 6I and movie S4). This phenomenon is likely due to the "fence" effect, where the membrane skeleton forms submicrometer compartments that restrict free diffusion (*27*). In contrast, filopodia did not exhibit similar confined or hopping behaviors (Fig. 6J and movie S5). This difference is likely due to the lower density of fence structures and higher membrane fluidity in filopodia, which need to rapidly respond to external stimuli and swiftly change shape to fulfill their exploratory and sensing functions (*29*).

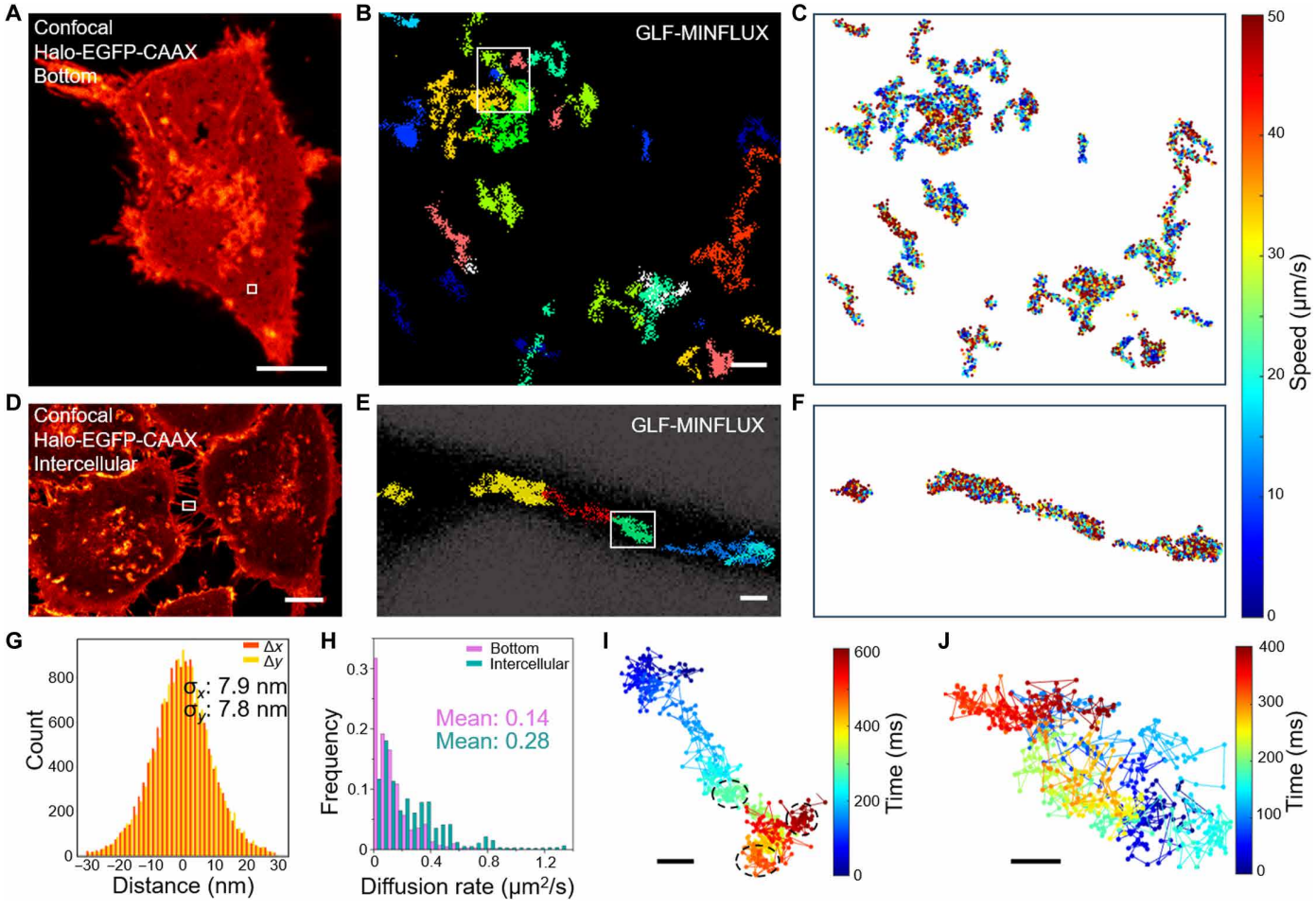

Fig. 6. Tracking in live cell membranes by GLF-MINFLUX. (**A**) Confocal image of the membrane at the basal surface of HeLa cells. (**B**) Single-molecule trajectories within the white box outlined in (A). Different colors represent distinct single-molecule tracks. (**C**) Velocities heatmap of all localization points from the trajectories shown in (B). The color bar maps velocity values. (**D**) Confocal image of the intercellular filopodia membrane. (**E**) Single-molecule trajectories within the white box outlined in (D). Different colors represent distinct single-molecule tracks. (**F**) Velocities heatmap of all localization points from the trajectories shown in (E). (**G**) Histograms of the SDs of lateral displacements Δ*x* and Δ*y* for consecutive localizations. (**H**) Histogram of diffusion rates for membrane proteins on the basal surface and intercellular filopodia. Diffusion rates are calculated as mean squared displacement divided by the time interval. (**I** and **J**) Temporal progression of the trajectory within the boxed region of B (I) and E (J). The color bar variations denote time points, illustrating the movement over time. The areas enclosed by the dashed black lines highlight regions exhibiting pronounced confined diffusion behavior. Scale bars, 10 μm [(A) and (D)], 200 nm [(B) and (E)], and 50 nm [(I) and (J)].

DISCUSSION

MINFLUX theoretically can achieve a localization precision of ~1 to 2 nm, but this level of precision is often challenging to attain in practical applications with biological samples, and very different labeling methods should be performed separately to achieve MINFLUX imaging or tracking. We, thus, introduce a general method: GLF-MINFLUX. In GLF-MINFLUX, the number of on fluorescent targets can be effectively regulated by simply varying the probe concentration without necessitating specific buffers or activation lasers. To ensure minimal background in GLF-MINFLUX under wash-free conditions, probes such as MaP618m-tubulin with over 200-fold fluorogenicity were synthesized. Such a high-contrast labeling from fluorogenic probes substantially benefits single-molecule localization during MINFLUX acquisition.

The combination of sequential illumination of targets by gradual labeling and the high fluorogenicity of MaP probes minimizes the occurrence of multiple emitters mimicking single-molecule emissions. GLF-MINFLUX achieves an impressive 2.6-nm localization precision, which is 1.7-fold greater than that of MINFLUX with Alexa Fluor 647 (Fig. 2E). The strong excitation laser also efficiently bleaches fluorescence after the labeling-locating event, ensuring that each protein is positioned only once. Meanwhile, in GLF-MINFLUX, the segmentation of densely packed structures into sparsely labeled subgroups substantially reduce invalid localizations during MINFLUX acquisition, offering more intact microtubule structures within 1.5 hours, whereas conventional one-step labeling with Alexa Fluor 647 only localized discontinuous microtubules. The labeling-locating-bleaching process in GLF-MINFLUX enables precise positioning of nearby targets within the localization precision limit, offering potential for quantitative analysis, provided that labeling efficiency is determined. In addition, it prevents interference from coactivation and quenching among adjacent fluorophores. GLF-MINFLUX, thus, enables the imaging of densely packed proteins that have not been achieved in previous studies, providing 3D information on TOM20 proteins with a spatial distance as small as 2.7 nm and dual-channel MINFLUX imaging of neuronal microtubules and microfilaments with 4.5- and 4.3 nm localization precision (Figs. 3 and 5 and table S3).

GLF-MINFLUX excels not only in nanoscale imaging but also in single-protein tracking of densely packed structures, without the need for washing steps. Traditional tracking techniques often rely on high photon counts from probes, sometimes using nanoparticles that are much larger than the target proteins, raising concerns about their fidelity in representing the native cellular state (*15*, *30*–*32*). Meanwhile, tedious washing steps are required to avoid the fluorescence from unspecific staining. While photoconvertible proteins, such as mEos2, enable MINFLUX tracking in live cells (*3*), organic fluorophores with better photostability and brightness could provide longer tracking duration (*33*). GLF-MINFLUX, using MaP618m dyes, allows for tracking of intracellular membrane proteins in living cells with exceptional spatial (7.8 nm) and temporal (200 μs) resolution (Fig. 6). This enables precise analysis of membrane fluidity and provides insights into diverse diffusion behaviors and rates across different cellular regions, which also provides great potential for tracking and studying intracellular proteins.

In GLF-MINFLUX, each cycle of MINFLUX imaging is performed within a time interval of 13 to 20 min, allowing single-molecule separation and localization with fewer invalid localizations (fig. S12). However, the localization speed gradually decreases in each cycle, unnecessarily prolonging the total acquisition time. Consequently, the manual replacement of fresh probes between cycles is required and must be carefully performed, as it may induce focal plane changes that could compromise the exceptional localization precision of MINFLUX imaging. Thus, a commercially available microfluidic buffer perfusion system, capable of automated, controllable, and GLF at the required concentration, could be seamlessly integrated into GLF-MINFLUX nanoscopy and would be highly beneficial, particularly for multichannel imaging. In addition, although the binding between MaP618m-tubulin and MaP618m-actin with microtubules and F-actins is sufficiently strong for enabling GLF-MINFLUX imaging, incorporating covalent bonds in future fluorogenic probes would further enhance precision in imaging. Meanwhile, GLF-MINFLUX has limitations, including relatively low sample efficiency due to the one-step labeling process that results in labeling all cells during the imaging of a single region, and the need for additional labeling, such as an auxiliary 488 nm channel, to localize the sample before imaging, both of which require further optimization.

In summary, GLF-MINFLUX offers a general labeling approach for nanoscale imaging and tracking of dense samples by improving localization precision. This methodology precisely controls the number of illuminated targets for MINFLUX nanoscopy via simply changing probe concentration, thereby eliminating the need for complex buffer systems or dedicated activation lasers and providing an easy-to-use experimental method. GLF-MINFLUX holds great promise for providing molecular-level insights into the organizations and functions of proteins in densely packed biological structures.

MATERIALS AND METHODS

Probe synthesis and characterization

Methods for organic synthesis and additional characterization can be found in the Supplementary Materials.

In vitro measurement of fluorescence spectroscopy

Absorption and emission spectra were measured on a BioTek Cytation 5 Cell Imaging Multimode Reader using a 384-well plate (no. 781090, Greiner) with an optical bottom. MaP618m-tubulin (1 mM in dimethyl sulfoxide) was diluted to 1 μM in tubulin buffer with or without tubulin protein (2 mg/ml; catalog no. T240, Cytoskeleton Inc.) and 0.1% SDS for control. The tubulin buffer also contained 80 mM Pipes (pH 6.9), 2 mM $MgCl_2$, 0.5 mM EGTA, 1 mM guanosine 5′-triphosphate (catalog no. BST06, Cytoskeleton Inc.), and 10% glycerol. The tubulin assay was incubated at 37°C for 2 hours before the absorption and emission spectra were measured. The absorption spectra were collected from 400 to 700 nm with a 2-nm sliding window, while the emission spectra under excitation at 595 nm were obtained from 625 to 700 nm with a 2-nm sliding window. All measurements were taken at ambient temperature (25° ± 2°C) in tubulin buffer, unless otherwise noted.

Cell lines culture

The pLVX-EGFP-Halo-Tubulin, pLVX-TOM20-Halo-EGFP, and Halo-EGFP-CAAX plasmids were stably transfected into BS-C-1 or HeLa cells via viral packaging, accompanied by two auxiliary plasmids, namely, psPAX2 (plasmid no. 12260, Addgene) and pMD2.G (plasmid no. 12259, Addgene). BS-C-1 cells [American Type Culture Collection (ATCC), CCL-26, BeNa Culture Collection, China) were cultured in minimum essential medium (11095-080, Gibco)

supplemented with 10% fetal bovine serum (FBS) (10099-141, Gibco), penicillin (100 U/ml), streptomycin (100 μg/ml; 15140-122, Gibco), and nonessential amino acids (11140-050, Gibco). Human embryonic kidney–293T (ATCC, CRL-3216, BeNa Culture Collection, China) and HeLa cells (ATCC, CCL-2, BeNa Culture Collection, China) were cultured in Dulbecco's modified Eagle's medium (DMEM) (11995-065, Gibco) supplemented with 10% FBS, penicillin (100 U/ml), and streptomycin (100 μg/ml). Cells were plated on cell culture dishes at 37°C with 5% CO_2. For live-cell tracking experiments, coverslips were incubated with gold nanorods (A12-40-980-CTAB-DIH-1-25, Nanopartz Inc.) for 30 min to serve as fiducial markers. Unbound nanorods were removed by washing the coverslips three times with water. Stable HeLa cells expressing Halo-EGFP-CAAX were seeded onto these treated coverslips and cultured under standard conditions (37°C at 5% CO_2).

Neuron culture

Hippocampal neuron cultures were obtained from postnatal day 0 (P0) to P3 Wistar rats of both sexes. Specifically, the hippocampi were meticulously isolated and digested with 0.25% trypsin-EDTA (25200072, Gibco) at 37°C for 20 min. After centrifugation and removal of the supernatant, the cells were resuspended in complete DMEM. Subsequently, the cells were plated on coverslips coated with poly-D-lysine (100 μg/ml; A3890401, Gibco) according to the manufacturer's recommendations. Neuronal cultures were maintained in Neurobasal-A medium (10888-022, Gibco) supplemented with 2% B27 serum-free supplement (17504044, Gibco), 1% GlutaMAX (35050-061, Gibco), penicillin (100 U/ml), and streptomycin (100 μg/ml). The neurons were fed with a one-half–volume change of medium every 3 days.

Cell fixation and labeling with fluorogenic probes

The cells were cultured for 1 day on 18 mm #1.0 coverslips (41001118, Deckglaser) placed in 12-well cell culture dishes. Cells expressing HaloTag were thoroughly rinsed with phosphate-buffered saline (PBS) or extraction buffer (100 mM Pipes, 1 mM EGTA, 1 mM $MgCl_2$, and 0.2% Triton X-100) for mitochondrial and microtubule imaging, respectively. Following fixation with 2.4% paraformaldehyde (157-8, Electron Microscopy Sciences) and 0.1% glutaraldehyde (16220, Electron Microscopy Sciences) for 10 min, the cells were rinsed three times with PBS, followed by an additional brief wash in PBS and immersion in a 10 mM sodium borohydride (71320, Sigma-Aldrich) solution in PBS for 5 min. Subsequently, the samples were washed with PBS and labeled with fiducial markers (gold nanorods, A12-40-980-CTAB-DIH-1-25, Nanopartz Inc.). The resulting gold nanorod solution was diluted by a 1:3 ratio in PBS and sonicated for 5 to 10 min. The coverslips were incubated with the nanorod solution and 1 mM dithiothreitol (DTT) for 15 min, and floating nanorods were removed through multiple PBS washes.

For labeling with MaP618-tubulin and MaP618-actin, the cells were permeabilized for 90 s in extraction buffer. Subsequently, the cells were incubated with 0.2% glutaraldehyde in PEM (100 mM Pipes, 1 mM EGTA, and 2 mM $MgCl_2$) for 15 min, followed by a brief wash in PEM and reduction in 10 mM sodium borohydride in PEM for 5 min. Next, the samples were subjected to three washes with PEM, and gold nanorods in PEM were introduced as previously described. The removal of floating nanorods was achieved through multiple washes with PEM. Before imaging, the coverslip containing the sample was fixed to the bottom of a dish with a central opening. Notably, freshly fixed samples, rather than aged preparations, should be used to ensure optimal labeling efficiency.

MINFLUX imaging

HaloTag-expressing cells that had been soaked in 1 mM DTT in PBS or PEM were immersed in a dish that was securely fixed to the specimen holder. An Abberior MINFLUX microscope (Abberior Instruments) equipped with a 1.4 numerical aperture, 100× oil objective lens and avalanche photodiodes was used for data acquisition. In accordance with the protocols outlined in preceding publications, the MINFLUX microscope underwent calibration before its utilization, ensuring optimal performance and reliability of the acquired data (*2*). Using Imspector software (v.16.3.15636-m2205-win64-MINFLUX, Abberior Instruments), cells were identified through a 488-nm confocal scan and brought into focus. Once the cells were in focus, the stabilization system of the microscope was activated, ensuring a stabilization precision that was generally below 1 nm. A region of interest was designated in the confocal scan image, and the 642-nm excitation laser power was set to 293 μW. The recording channel was adjusted to 650 to 685 nm. Because the background noise in this method is exceptionally low and has minimal dependence on pinhole diameter, all data collection was performed using the default pinhole diameter of 0.78 airy units (AU). Subsequently, appropriate sequences were chosen for data acquisition. The fixed cells were stained with fluorogenic MaP dyes, adjusting the concentration according to the field of view before imaging. Fresh probe solution was replenished every 10 to 15 min to maintain the acquisition rate. For fixed cells labeled with Alexa Fluor 647, sample preparation and subsequent MINFLUX imaging were carried out following the methodologies outlined in preceding publications (*9*). This included the introduction of reductive and oxidative imaging buffer to facilitate the blinking of the fluorophores, enabling the acquisition of high-precision localization data. For dual channel imaging, we used a sequential addition method for data acquisition. Specifically, this involved initially introducing one type of probe, followed by completing the signal acquisition for that probe. Subsequently, the sample was washed and subjected to photobleaching to ensure the removal of any remaining active probes. Only after confirming the absence of new localization signals was the next type of probe added. This approach guarantees that the signals from each probe are independent and clear, thereby preventing cross-contamination or signal overlap. For the tracking experiments, after identifying the optimal field of view using the 488 channel and stabilizing the focal plane, the tracking iteration sequence was selected, and data were collected following the predetermined probe concentration (10 pM). Because of the lack of an active cell maintenance system on the instrument, each cell was kept outside the incubator for no more than 20 min. Conventional MINFLUX with mEos2 yields around 500 localization points (*3*), while GLF-MINFLUX allows for approximately 1000 localization points (Fig. 6), enabling longer tracking durations.

MINFLUX data analysis

Data were exported in MSR (measurement data file) and MAT (MATLAB MAT-file) formats to allow them to be analyzed in various software platforms. The exported files contained all the recorded parameters for both valid localizations and discarded invalid attempts. MSR files were used to directly visualize confocal images and the presentation of MINFLUX localization distributions. MAT

files, which are compatible with MATLAB (2022b), were used for the automated computation of the localization precision, CFR, t_{btw}, f_{bg}, and other parameters through customized analysis scripts. For all the computational analyses, only the data from the final MINFLUX iteration were used. The localization precision was estimated from experimental data by aligning the mean value of all localization groups acquired from individual emission bursts. A Gaussian function was fit to the resulting histogram, providing an estimate of the localization precision. The characterization and specific calculation of the parameters CFR, t_{btw}, and f_{bg} align with previously described methodologies (*5*). The localization precision for tracking is determined by calculating the differences between consecutive points in the x and y directions separately. The variance of these differences is then computed, and the square root of this variance yields the localization precision.

MINFLUX sequences

Data acquisition for the MINFLUX microscope was conducted according to a predefined set of parameters detailed in a text file (see data S1 to S3). These parameters delineated a sequential framework governing the iterative amplification of single-molecule events. The MINFLUX iteration process includes one prelocalization iteration and four additional iterations in 2D space (Table 1). The 3D experiments include one prelocalization iteration and nine additional iterations (Table 2). The tracking process includes one prelocalization iteration and three additional iterations (Table 3).

Image rendering in two dimensions

To obtain time-series images, MATLAB scripts were used to simplify the aggregation of valid localizations across different time intervals. Localizations counts from each interval were converted into grayscale images with pixel sizes of 10 and 2 nm, which allowed for a high-resolution representation of the localization events. Subsequently, ImageJ was used for processing and visualization of these grayscale images, enabling quantitative analysis and qualitative visualization of the data. For other images, the Imspector software was used to depict valid localization events. This software allowed for the presentation of these events as 2D grayscale maps with various pixel sizes. The high-resolution grayscale maps generated by Imspector provided a detailed visualization of the spatial distribution of localization events over time, which facilitated further analysis and interpretation of the data.

Image rendering in three dimensions

First, MINFLUX-derived data were imported into ParaView (5.8.1-Windows-Python3.7-msvc2015-64bit). Then, each localization event was substituted with a Gaussian distribution and visually depicted with chromatic coding based on the z-axis value. Images were systematically rotated in the built-in 3D viewer to capture snapshots from diverse orientations and subsequently amalgamated into an animation. Then, the MINFLUX dataset was imported into MATLAB, where localization clouds representing corresponding to distinct events were marked with distinct colors. The targeted regions of interest were then isolated and represented using MATLAB's 3D scatter plot function, facilitating comprehensive exploration and analysis.

Determining the central point of each emitter

Upon importing the MINFLUX data into MATLAB, a unique identifier (Tid) was assigned to each event, allowing for the systematic analysis of the corresponding data. MATLAB scripts were used to calculate the center points of the localization clouds for each event, based on the variance of each localization coordinate. These center points served as an estimate of the centroids for each emitter, reflecting the most likely position of the emitter within the localization cloud. By replacing the original localizations with these derived center points, it became possible to precisely determine the spatial positions and quantities of individual probes within the sample, thereby enhancing the precision and resolution of the imaging data.

Mapping the mitochondrial protein distribution

Mitochondria were conceptualized as flat cylinders on the xy plane. Using customized software with coordinate adjustment capability, the major axis of the cylinder was aligned with the x axis. We also shifted the cylinder along the z axis to ensure that the center of the cross-sectional view coincided with the origin of the z axis. The extraneous points along the mitochondrial circumference were systematically removed, resulting in a refined representation. The angles between each protein and the y axis were computed on the basis of the y and z coordinate information, where 0 or π corresponded to the two sides of the mitochondria, $\pi/2$ corresponded to the upper surface, and $-\pi/2$ corresponded to the lower surface.

Estimation of microtubule diameter

To ensure an objective evaluation, we used an automated image processing software called Line Profiler for the statistical analysis of microtubule diameters (*34*). Line Profiler automatically evaluates potential regions of interest along filamentous structures to generate cross-sectional profiles, which are then fitted by the sum of two Gaussian functions to determine the peak-to-peak distance across the section.

Supplementary Materials

The PDF file includes:

Supplementary Text S1 to S10
Figs. S1 to S17
Tables S1 to S3
Legends for movies S1 to S5
Legends for data S1 to S3

Other Supplementary Material for this manuscript includes the following:

Movies S1 to S5
Data S1 to S3

REFERENCES AND NOTES

1. S. J. Sahl, J. Matthias, K. Inamdar, M. Weber, T. A. Khan, C. Brüser, S. Jakobs, S. Becker, C. Griesinger, J. Broichhagen, S. W. Hell, Direct optical measurement of intramolecular distances with angstrom precision. *Science* **386**, 180–187 (2024).
2. R. Schmidt, T. Weihs, C. A. Wurm, I. Jansen, J. Rehman, S. J. Sahl, S. W. Hell, MINFLUX nanometer-scale 3D imaging and microsecond-range tracking on a common fluorescence microscope. *Nat. Commun.* **12**, 1478 (2021).
3. F. Balzarotti, Y. Eilers, K. C. Gwosch, A. H. Gynnå, V. Westphal, F. D. Stefani, J. Elf, S. W. Hell, Nanometer resolution imaging and tracking of fluorescent molecules with minimal photon fluxes. *Science* **355**, 606–612 (2017).
4. K. C. Gwosch, J. K. Pape, F. Balzarotti, P. Hoess, J. Ellenberg, J. Ries, S. W. Hell, MINFLUX nanoscopy delivers 3D multicolor nanometer resolution in cells. *Nat. Methods* **17**, 217–224 (2020).
5. L. M. Ostersehlt, D. C. Jans, A. Wittek, J. Keller-Findeisen, K. Inamdar, S. J. Sahl, S. W. Hell, S. Jakobs, DNA-PAINT MINFLUX nanoscopy. *Nat. Methods* **19**, 1072–1075 (2022).
6. C. P. Grabner, I. Jansen, J. Neef, T. Weihs, R. Schmidt, D. Riedel, C. A. Wurm, T. Moser, Resolving the molecular architecture of the photoreceptor active zone with 3D-MINFLUX. *Sci. Adv.* **8**, eabl7560 (2022).

7. Y. Eilers, H. Ta, K. C. Gwosch, F. Balzarotti, S. W. Hell, MINFLUX monitors rapid molecular jumps with superior spatiotemporal resolution. *Proc. Natl. Acad. Sci. U.S.A.* **115**, 6117–6122 (2018).
8. G. T. Dempsey, J. C. Vaughan, K. H. Chen, M. Bates, X. Zhuang, Evaluation of fluorophores for optimal performance in localization-based super-resolution imaging. *Nat. Methods* **8**, 1027–1036 (2011).
9. J. K. Pape, T. Stephan, F. Balzarotti, R. Büchner, F. Lange, D. Riedel, S. Jakobs, S. W. Hell, Multicolor 3D MINFLUX nanoscopy of mitochondrial MICOS proteins. *Proc. Natl. Acad. Sci. U.S.A.* **117**, 20607–20614 (2020).
10. R. Lincoln, M. L. Bossi, M. Remmel, E. D'Este, A. N. Butkevich, S. W. Hell, A general design of caging-group-free photoactivatable fluorophores for live-cell nanoscopy. *Nat. Chem.* **14**, 1013–1020 (2022).
11. T. S. Mihaila, C. Bäte, L. M. Ostersehlt, J. K. Pape, J. Keller-Findeisen, S. J. Sahl, S. W. Hell, Enhanced incorporation of subnanometer tags into cellular proteins for fluorescence nanoscopy via optimized genetic code expansion. *Proc. Natl. Acad. Sci. U.S.A.* **119**, e2201861119 (2022).
12. A. Aktalay, T. A. Khan, M. L. Bossi, V. N. Belov, S. W. Hell, Photoactivatable carbo- and silicon-rhodamines and their application in MINFLUX nanoscopy. *Angew. Chem. Int. Edit.* **62**, e202302781 (2023).
13. M. Remmel, L. Scheiderer, A. N. Butkevich, M. L. Bossi, S. W. Hell, Accelerated MINFLUX nanoscopy, through spontaneously fast-blinking fluorophores. *Small* **19**, e2206026 (2023).
14. R. T. Gerasimaitė, J. Bucevičius, K. A. Kiszka, S. Schnorrenberg, G. Kostiuk, T. Koenen, G. Lukinavičius, Blinking fluorescent probes for tubulin nanoscopy in living and fixed cells. *ACS Chem. Biol.* **16**, 2130–2136 (2021).
15. J. O. Wirth, L. Scheiderer, T. Engelhardt, J. Engelhardt, J. Matthias, S. W. Hell, MINFLUX dissects the unimpeded walking of kinesin-1. *Science* **379**, 1004–1010 (2023).
16. A. Ghosh, M. Meub, D. A. Helmerich, P. Eiring, K. M. Kortüm, S. Doose, M. Sauer, Decoding the molecular interplay of endogenous CD20 and rituximab with fast volumetric nanoscopy. bioRxiv 2023.10.09.561472 [Preprint] (2023). https://doi.org/10.1101/2023.10.09.561472.
17. E. A. Katrukha, D. Jurriens, D. M. S. Pastene, L. C. Kapitein, Quantitative mapping of dense microtubule arrays in mammalian neurons. *eLife* **10**, e67925 (2021).
18. L. Wang, M. Tran, E. D'Este, J. Roberti, B. Koch, L. Xue, K. Johnsson, A general strategy to develop cell permeable and fluorogenic probes for multicolour nanoscopy. *Nat. Chem.* **12**, 165–172 (2020).
19. Y. Araiso, T. Endo, Structural overview of the translocase of the mitochondrial outer membrane complex. *Biophys. Physicobiol.* **19**, e190022 (2022).
20. S. Stoldt, T. Stephan, D. C. Jans, C. Brüser, F. Lange, J. Keller-Findeisen, D. Riedel, S. W. Hell, S. Jakobs, Mic60 exhibits a coordinated clustered distribution along and across yeast and mammalian mitochondria. *Proc. Natl. Acad. Sci. U.S.A.* **116**, 9853–9858 (2019).
21. F. Xu, D. Ma, K. P. MacPherson, S. Liu, Y. Bu, Y. Wang, Y. Tang, C. Bi, T. Kwok, A. A. Chubykin, P. Yin, S. Calve, G. E. Landreth, F. Huang, Three-dimensional nanoscopy of whole cells and tissues with in situ point spread function retrieval. *Nat. Methods* **17**, 531–540 (2020).
22. S. C. Reinhardt, L. A. Masullo, I. Baudrexel, P. R. Steen, R. Kowalewski, A. S. Eklund, S. Strauss, E. M. Unterauer, T. Schlichthaerle, M. T. Strauss, C. Klein, R. Jungmann, Ångström-resolution fluorescence microscopy. *Nature* **617**, 711–716 (2023).
23. K. Weber, P. C. Rathke, M. Osborn, Cytoplasmic microtubular images in glutaraldehyde-fixed tissue culture cells by electron microscopy and by immunofluorescence microscopy. *Proc. Natl. Acad. Sci. U.S.A.* **75**, 1820–1824 (1978).
24. C. Leterrier, A pictorial history of the neuronal cytoskeleton. *J. Neurosci.* **41**, 11–27 (2021).
25. M. Mikhaylova, B. M. Cloin, K. Finan, R. Van Den Berg, J. Teeuw, M. M. Kijanka, M. Sokolowski, E. A. Katrukha, M. Maidorn, F. Opazo, Resolving bundled microtubules using anti-tubulin nanobodies. *Nat. Commun.* **6**, 7933 (2015).
26. C. Conze, N. I. Trushina, M. Holtmannspötter, M. Rierola, S. Attanasio, L. Bakota, J. Piehler, R. Brandt, Super-resolution imaging and quantitative analysis of microtubule arrays in model neurons show that epothilone D increases the density but decreases the length and straightness of microtubules in axon-like processes. *Brain Res. Bull.* **190**, 234–243 (2022).
27. A. Kusumi, C. Nakada, K. Ritchie, K. Murase, K. Suzuki, H. Murakoshi, R. S. Kasai, J. Kondo, T. Fujiwara, Paradigm shift of the plasma membrane concept from the two-dimensional continuum fluid to the partitioned fluid: High-speed single-molecule tracking of membrane molecules. *Annu. Rev. Biophys.* **34**, 351–378 (2005).
28. L. P. Wright, M. R. Philips, Thematic review series: Lipid posttranslational modifications CAAX modification and membrane targeting of Ras. *J. Lipid Res.* **47**, 883–891 (2006).
29. W. Y. Lam, Y. Wang, B. Mostofian, D. Jorgens, S. Kwon, K. Chin, M. A. Carpenter, T. Jacob, K. Heiser, A. Agrawal, HER2 cancer protrusion growth signaling regulated by unhindered, localized filopodial dynamics. bioRxiv 654988 [Preprint] (2019). https://doi.org/10.1101/654988.
30. X. Nan, P. A. Sims, X. S. Xie, Organelle tracking in a living cell with microsecond time resolution and nanometer spatial precision. *ChemPhysChem* **9**, 707–712 (2008).
31. F. Cole, J. Zähringer, J. Bohlen, T. Schröder, F. Steiner, M. Pfeiffer, P. Schüler, F. D. Stefani, P. Tinnefeld, Super-resolved FRET and co-tracking in pMINFLUX. *Nat. Photonics* **18**, 478–484 (2024).
32. T. Deguchi, M. K. Iwanski, E.-M. Schentarra, C. Heidebrecht, L. Schmidt, J. Heck, T. Weihs, S. Schnorrenberg, P. Hoess, S. Liu, V. Chevyreva, K. M. Noh, L. C. Kapitein, J. Ries, Direct observation of motor protein stepping in living cells using MINFLUX. *Science* **379**, 1010–1015 (2023).
33. C. Schirripa Spagnolo, S. Luin, Choosing the probe for single-molecule fluorescence microscopy. *Int. J. Mol. Sci.* **23**, 14949 (2022).
34. F. U. Zwettler, S. Reinhard, D. Gambarotto, T. D. Bell, V. Hamel, P. Guichard, M. Sauer, Molecular resolution imaging by post-labeling expansion single-molecule localization microscopy (Ex-SMLM). *Nat. Commun.* **11**, 3388 (2020).

Acknowledgments

Funding: M.G. was supported by the Shanghai Municipal Science and Technology Major Project and the Shanghai Frontiers Science Center Program (grant 2021-2025 no. 20). L.W. was supported by the National Natural Science Foundation of China (22477016 and 32171360), the National Key R&D Program of China (2024YFA1307400), and the Basic Research Special Zone Plan of Shanghai (22TQ020). J.M. was supported by the National Key R&D Program of China (2021YFF0502900), the National Natural Science Foundation of China (62175034), the Science and Technology Research Program of Shanghai (grant no. 19DZ2282100), the Shanghai Key Laboratory of Metasurfaces for Light Manipulation (23dz2260100), and the Shanghai Engineering Technology Research Center of Hair Medicine (19DZ2250500). Q.Z. was supported by the Shanghai Science and Technology Innovation Action Plan (grant nos. 23JC1403100 and 24JD1402700). **Author contributions:** Conceptualization: M.G., L.Y., L.W., and J.M. Methodology: L.Y., D.S., J.M., and L.W. Investigation: L.Y., D.S., and J.M. Resources: L.Y. and D.S. Validation: L.Y., L.W., and J.M. Data curation: L.Y., L.W., J.M., L.C., and S.L. Formal analysis: L.Y., D.S., J.M., S.L., and J.G. Software: L.Y., S.L., and L.C. Visualization: L.Y., D.S., S.L., J.W., L.W., and J.M. Project administration: M.G., L.Y., L.W., and J.M. Supervision: M.G., L.Y., J.W., L.W., and J.M. Writing—original draft: L.Y., D.S., and L.W. Writing—review and editing: M.G., L.Y., L.W., J.M., J.W., and Q.Z. Funding acquisition: M.G., Q.Z., L.W., and J.M. **Competing interests:** L.W. is an inventor on a patent application related to this work (WO2020115286A2, Max-Planck Institute for Medical Research, 6 December 2019). The authors declare that they have no other competing interests. **Data and materials availability:** All data needed to evaluate the conclusions in the paper are present in the paper and/or the Supplementary Materials.

Submitted 27 December 2024
Accepted 17 April 2025
Published 21 May 2025
10.1126/sciadv.adv5971